



Architecture-inspired paradigm for 3D bioprinting of vessel-like structures using extrudable carboxylated agarose hydrogels

Aurelien Forget¹ · Tiziano Derme² · Daniela Mitterberger³ · Markus Heiny¹ · Caleb Sweeney⁴ · Likhith Mudili⁴ · Tim R. Dargaville⁴ · V. Prasad Shastri¹

Received: 3 June 2019 / Accepted: 10 July 2019
© Qatar University and Springer Nature Switzerland AG 2019

Abstract

3D bioprinting as a process has enabled the creation of complex structures laden with biological information including cells that is not realizable with conventional manufacturing techniques. Within this new manufacturing process, design strategies and design tools have to be adapted to deliver its full potential. In architecture, parametric design has allowed the creation of new shapes by expressing parameters in an algorithm that defines the relationship between design intent and design response. In this study, the application of this method to the bioprinting of hollow channel grown in silico within a porous scaffold is demonstrated. The final object was printed using a novel bioink formulation based on carboxylated agarose that is extrudable at ambient temperature. The hollow bioprinted object was imaged with X-ray computed tomography to obtain a 3D model for design validation. This proposed workflow “from design to validation” represents a new paradigm for realizing complex structures in 3D bioprinting through in silico optimization.

1 Introduction

One of the primary objectives of 3D bioprinting, an additive manufacturing process, is to generate through mimicry of tissue macro- and micro-architecture, “functional” tissue, and tissue-like structures (organoids) for transplantation and ex vivo drug screening. In an ex vivo setting, the establishment of a channel network is essential to deliver the required nutrients for cells to grow and function. In vivo, in order for

bioprinted organs to become functional, they need to be vascularized. In this regard, a priori channels to accommodate the ingress of blood vessels need to be designed within the blueprint of the organ to be printed. In order for efficient exchange of nutrients, oxygen, and waste which is essential for the survival and growth of a transplanted tissue, cells need to be in close vicinity to blood vessels in order to overcome diffusional limits. Current approaches for the design of blood vessel networks in 3D bioprinting have focused on replicating the channel architecture used in microfluidics which is sequential convergent and divergent branching of parallel lines, or simple square patterns [1, 2], or reproduction of natural arterial structure obtained from imaging modalities such as magnetic resonance imaging (MRI) [3]. However, the branching of blood vessels follows a fractal pattern and realizing the shape and path of blood vessels in vitro in bioprinting is comparable to an architectural challenge consisting of connecting a starting point to an endpoint through a defined topography using a road or channel. Therefore, a similar approach and tools used in architecture could be applied to the design of voids within 3D-printed structures to accommodate the formation of blood vessels.

The diminishing cost of computational power, data storage, and the development of novel drawing software has offered new approaches for the intricate design of architectural and artistic objects. Among them, parametric design is a process

Electronic supplementary material The online version of this article (<https://doi.org/10.1007/s42247-019-00045-5>) contains supplementary material, which is available to authorized users.

- ✉ Aurelien Forget
aurelien.forget@makro.uni-freiburg.de
- ✉ V. Prasad Shastri
prasad.shastri@gmail.com; prasad.shastri@makro.uni-freiburg.de

- ¹ Institute for Macromolecular Chemistry, University of Freiburg, Stefan-Meier Str. 31, 79104 Freiburg, Germany
- ² Institute for Experimental Architecture, University of Innsbruck, 6020 Innsbruck, Austria
- ³ Institute of Technology in Architecture, ETH, 8092 Zurich, Switzerland
- ⁴ Institute for Health and Biomedical Innovation, Queensland University of Technology, Brisbane 4001, Australia

based on algorithms that enable the expression of parameters and rules that define the design and that encodes the relationship between design intent and design response [4]. This means that instead of drawing the intended design in a conventional computer-assisted drawing (CAD) software through extrusion, revolution, and cuts, an algorithm creates the design following the rules and constraints defined by the user. This technique allows defining parameters that will result in a sophisticated design not possible, or difficult to achieve, through conventional drawing approaches. Parametric design has been used in 3D printing and enables the creation of complex design not possible with traditional computer-aided drawing approaches [5] for instance, for the design of bone implants [6]. This design approach can be applied to the design of blood vessels as well, as blood vessels show fractal branching and hence can be defined mathematically. Parameters are carefully selected to create channels within a given volume and through simple changes in the parameters; a multitude of paths can be designed and implemented.

This study proposes a strategy to grow *in silico* channels by applying parametric design, for the eventual design of blood vessel-like architecture. First, a porous scaffold is computed by mimicking mammalian fibrous tissues. Then, a channel is grown within this porous volume by finding its path through the pores of the scaffold. Using such an approach, two channels were designed and the printability of the created channels was tested using a biocompatible extrudable hydrogel. The channel was printed with Pluronic F-127, a hydrogel with a lower critical solution temperature (LCST) as a fugitive support [7] and an embedded feature in carboxylated agarose (CA) hydrogel, which was previously established as a biocompatible hydrogel for 3D cell culture [8, 9] and an excellent bioink for 3D bioprinting [10]. The object with a hollow perfusable channel realized by eluting the Pluronic fugitive phase was further characterized by X-ray computed tomography.

2 Results and discussion

2.1 *In silico* growth of blood vessel

Mammalian tissues are composed of various macromolecular polysaccharides and structural proteins such as collagen which make up the extracellular matrix (ECM). These macromolecules organize into fibers or 3D networks, forming what is essentially a hydrogel [11]. These tissues exhibit a specific porosity allowing cells to migrate and to organize into functional structures. Within tissues, blood vessels are one of the essential structures delivering the required nutrients and oxygen to the surrounding environment. The infiltration of blood vessels in tissue is governed by many biological processes such as chemokine gradients, morphogens, secretion of matrix

metalloproteinases that are able to degrade the ECM, and stiffness of the ECM [12, 13]. Also, physical properties of the extracellular matrix play a significant role. Parameters such as pore size [14] and pore connectivity [15] can influence blood vessel paths [16]. So, if we can model *in silico* some of the physical aspects of the ECM architecture, then we would be able to mimic the natural growth of blood vessels within a virtual model. To test this concept, we applied an algorithm-based approach. With this process, a synthetic blood vessel autonomously emerges by finding its path through a computer-modeled porous structure.

2.2 Scaffolding generation

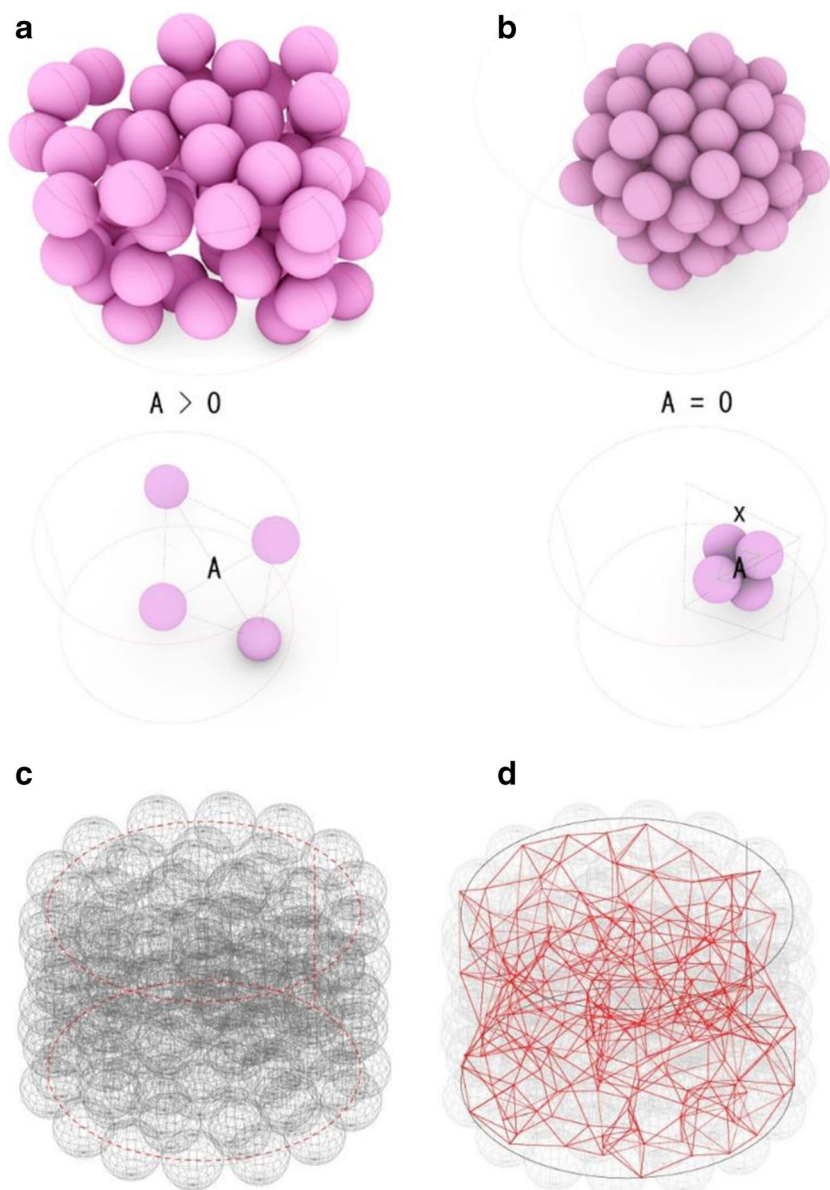
First, a porous scaffolding lattice is computed using a sphere-packing approach. Spheres of a given diameter are placed in a 16-mm diameter volume (Fig. 1a). Then, an algorithm calculates an optimal spatial network by compacting the spheres without overlapping (Fig. 1b). This calculation resulted in a cylindrical volume fully packed with the spheres (Fig. 1c). Next, the creation of the spatial structure was computed by triangulating the center of each sphere with a group of neighboring others (Fig. 1d). This process gave a homogenous network of triangles with a constant average area and the possibility to evaluate and tune the desired porous structure [17]. The final resolution of the scaffolding was obtained using an iso-surfacing algorithm and generated a rough volumetric data from 2D information (lines or points).

Two networks were generated with a pore size in which, through the density of the arrangement of the spheres, it was possible to approximate the size of the pores of the resulting scaffolding. The porosity of a scaffold is a measure of the average void volume and does not provide any information on how the pores are interconnected and whether the pores are open or closed [18]. With this process, two porous frames were computed: one with pores between 0.05 to 2 mm (Fig. 2a) and one with pores between 0.3 to 3.7 mm (Fig. 2b). The frames were then converted into volumetric scaffolds (Fig. 2c, d). These 3D scaffolds are then used as a restricting volume in which blood vessels can grow (Fig. 2e, f).

2.3 Vessel generation

Within the *in silico* ECM mimics, the biological channel was programmed to grow through the pores. The vessel's design for both scaffolds was generated using an agent-based system modeling behavior [19]. The single agent has a starting point and a target point at the top of the volume. Then, it moves through the scaffold with a series of two specific spatial constraints: collision avoidance and shortest path. The first condition describes the distance the agent needs to keep from the volumetric scaffolding, while the second refers to the agent's

Fig. 1 **a** Initial condition scaffolding generation (radii, boundary, number of members). **b** Sphere packing using constant radii and **c** optimization gradual reduction from the initial state to optimal pores size. **d** Isosurfacing, an operation commonly used in computer modeling to generate a rough volumetric data from 2D information (lines or points)



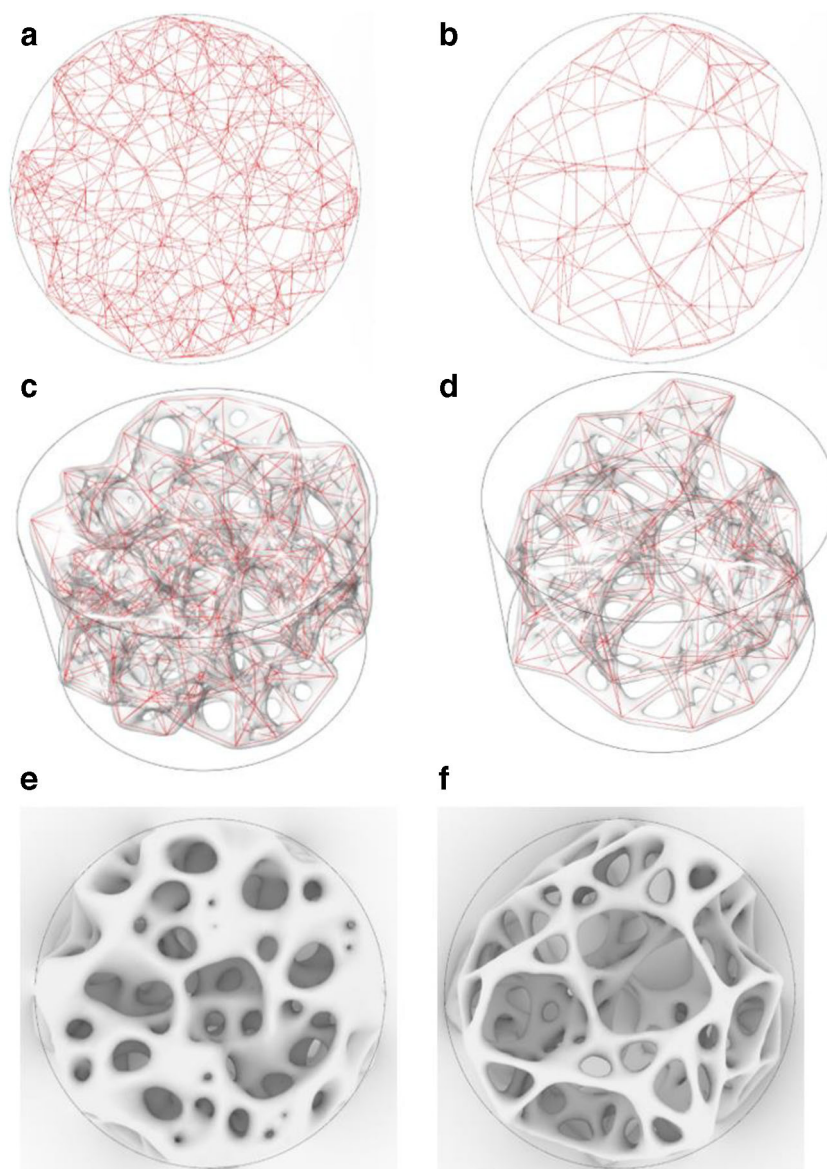
entropy to reach the endpoint using the shortest path rule. The behavior of a single agent proved beneficial for the reduction of the tortuosity of a vessel, underlining the relationship between a smaller tolerance of collision and an increment of tortuosity. In the *in silico* ECM mimics with an average value of 1.5-mm pore size, a 1-mm diameter channel was grown (Fig. 3a) while in the ECM mimics of 3.7-mm average pore size, a 3-mm diameter channel was grown (Fig. 3b). Each of the resulting vessels had a different path and shape, which could be observed in the wireframe representation of the construct (Fig. 3c, d). To characterize the vessels, the tortuosity of each vessel was estimated using the arc-chord ratio mathematical method: the ratio of the length of the curve to the distance between the ends of it. The grown vessels exhibited different tortuosity of 1.2 and 1.25 for the 1-mm and 3-mm channels,

respectively (Fig. 3e, f). Similar tortuosity in the vessels will enable the bioprinting of both vessels using identical bioprinting parameters.

2.4 Bioprinting workflow

To 3D print hollow structures, several approaches have been proposed. In a conventional fused deposition modeling process, removable support structures can be included in the design. Printed with a lower materials density than the printed part, the supports can be conveniently detached after printing [20]. Another approach consists of printing hollow parts in a support material such as hydrogel slurry, like agarose or gelatin, and this technique is known as the FRESH process [21]. Alternatively, fugitive materials can be used to fill the hollow

Fig. 2 Wireframe obtained from sphere packing for **a** the 1.5-mm pore size average scaffold and **b** the 3.7-mm pore size average scaffold. **c** and **d** Conversion of volumetric data to scaffolds. Resulting in silico ECM mimics for **e** the small pore size scaffold and **f** scaffold with larger pores

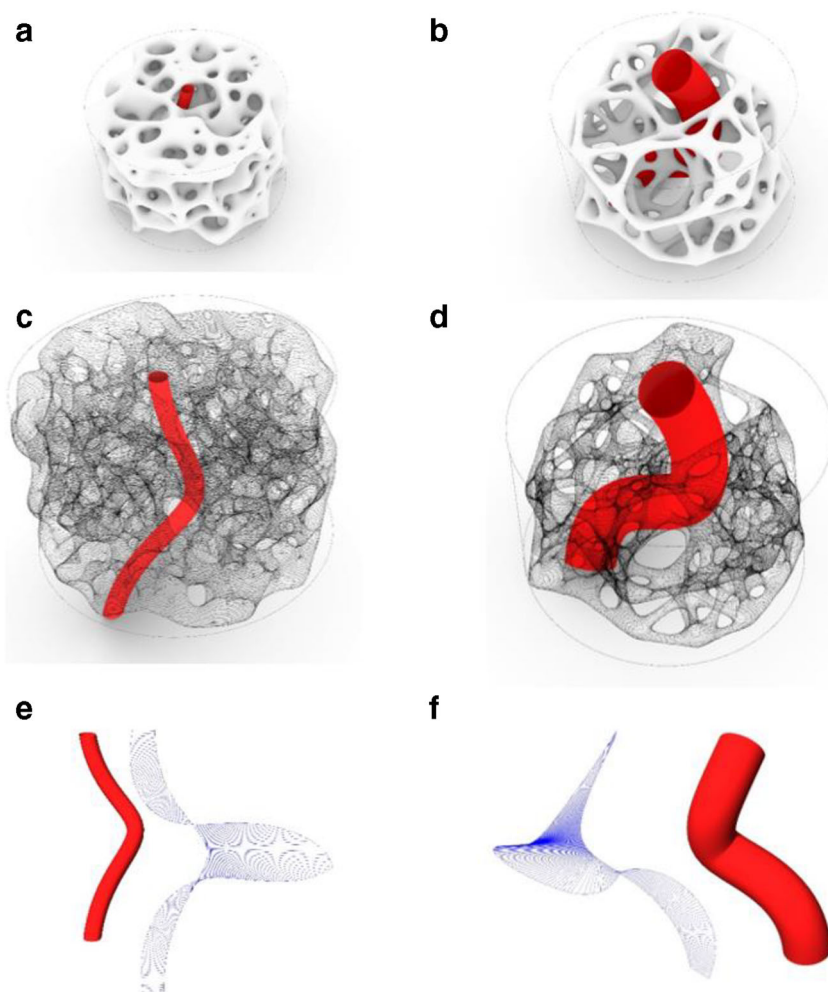


structures and then eluted with a solvent that is non-solvent for the printed material. However, for biological applications, cytotoxic solvents cannot be used [22]. To replace such solvents, bioprintable materials such as physical hydrogels that undergo a gel-to-solution transition below room temperature could be used as support materials to create hollow structures [23]. The poloxamer Pluronic F-127 which is a triblock copolymer of polypropylene oxide (PPO)-polyethylene oxide (PEO)-PPO, as proven very critical in bioprinting as it has a lower critical solution temperature (LCST) below room temperature and undergoes a gel-to-solution transition around 4 °C. In contrast, polysaccharide-derived physical gels such as agarose and its chemically modified counterpart, carboxylated agarose, exhibit a hysteresis behavior with a solution-to-gel transition below 37 °C and a corresponding gel-to-solution transition around 90 °C [24]. CA hydrogels are also extrudable and

biocompatible, and have been shown to support angiogenesis and stabilize blood vessels [25]. Here, we use the stability of CA hydrogels at low and room temperature, and the solubilization properties of Pluronic at low temperature to create a bioprintable system with a fugitive bioink. Hence, the Pluronic was used as a temperature-activated fugitive material embedded in the CA matrix. Both materials are bioprinted together with the Pluronic used to bioprint the vessel embedded in the CA. After incubation at 4 °C, the Pluronic phase can be removed, leaving a hollow path in a CA cylinder (Fig. 4a) [26].

The parametric design approach described herein allowed us to create two types of vessels: one with a 1-mm diameter and one with a 3-mm diameter. From the computed design, each of the channels was converted into two additive manufacturing compatible digital files: a cylindrical volume

Fig. 3 3D representation of the channel in the restricted geometry of **a** the vessel of 1-mm diameter generated using a scaffold with 1.5-mm average pores size and **b** the vessel of 3-mm diameter generated using a scaffold with 3.7-mm average pores size. Wire representation of the scaffold allowing to visualize the vessel path for **c** the 1-mm vessel and **d** the 3-mm vessel. A graphic representing the tortuosity of **e** the 1-mm vessels and **f** the 3-mm vessel



which will be bioprinted in the CA (Fig. 4b, c) and one vessel which will be bioprinted with the fugitive ink: Pluronic F-127 (Fig. 4d, e). Each file is then converted into a Gcode file that codes for the 3D bioprinter movement and controls the dual extrusion (Fig. 4f, g).

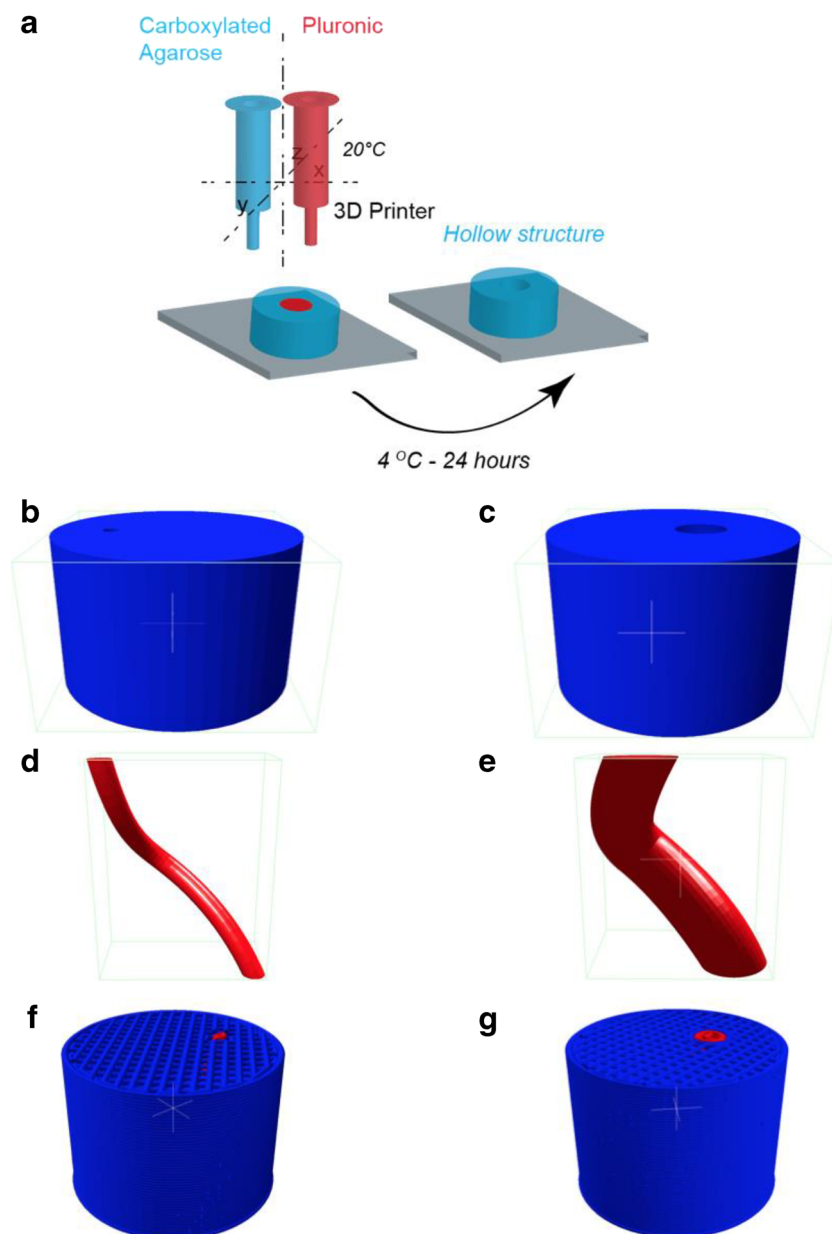
2.5 Shear-thinning properties of carboxylated agarose

We previously reported the bioprinting of carboxylated agarose (CA) using a drop-on-demand bioprinter [10]. There, the CA was extruded above the sol-gel temperature transition, i.e., as a liquid. This required that the CA solution be deposited on a cooled stage to promote instantaneously gelation; therefore, the process requires a heated extrusion head and a temperature-controlled stage. A biocompatible bioink amendable for extrusion at room temperature would be compatible with a wider range of bioprinters and applications. Therefore, we investigated the rheological properties of CA with three degrees of carboxylation as follows: 40%, 60%, and 80% (denoted CA40, CA60, and CA80, respectively) at ambient

temperature. We found out that independent of the polysaccharide concentration, CA hydrogels exhibited shear-thinning properties over a range of shear rate from 0.1 to 100 rad/s (Fig. 5a–c). This viscoelastic behavior might originate from the organization of CA into a β -sheet-like structure and its low intermolecular H-bond formation capabilities [27]. The shear-thinning behavior of CA hydrogels suggests that these hydrogels could be extruded at room temperature.

Extrusion of a viscoelastic material through a needle requires overcoming the adherence force of the materials with the container wall and disruption of the material organization to enable the material to flow [28]. The force required for extrusion is dependent on both the materials but the extrusion dies. In this study, three conical extrusion needles of 26, 30, and 32 G were employed (SI-Fig. 1A), which were mounted on a cylindrical cartridge containing the hydrogels (SI-Fig. 1B). Most laboratory 3D bioprinters are based on pneumatic elements, that is, they use compressed air to extrude the hydrogels. Therefore, a wiper type piston was used (SI-Fig. 1C). With this setup, we identified which combination of hydrogel formulation could be extruded on a standard laboratory

Fig. 4 a 3D bioprinting workflow of dual extrusion with Pluronic F-127 as fugitive ink. Volume converted into stereolithography (STL) files for the tissue around the **b** 1-mm vessel and **c** the 3-mm vessel. Corresponding 3D STL files for the **d** 1-mm vessel and **e** 3-mm vessel. Representation of the converted Gcode volumes (*blue*) and channels (*red*) used to control the 3D bioprinter for **f** the 1-mm vessel and **g** 3-mm vessel



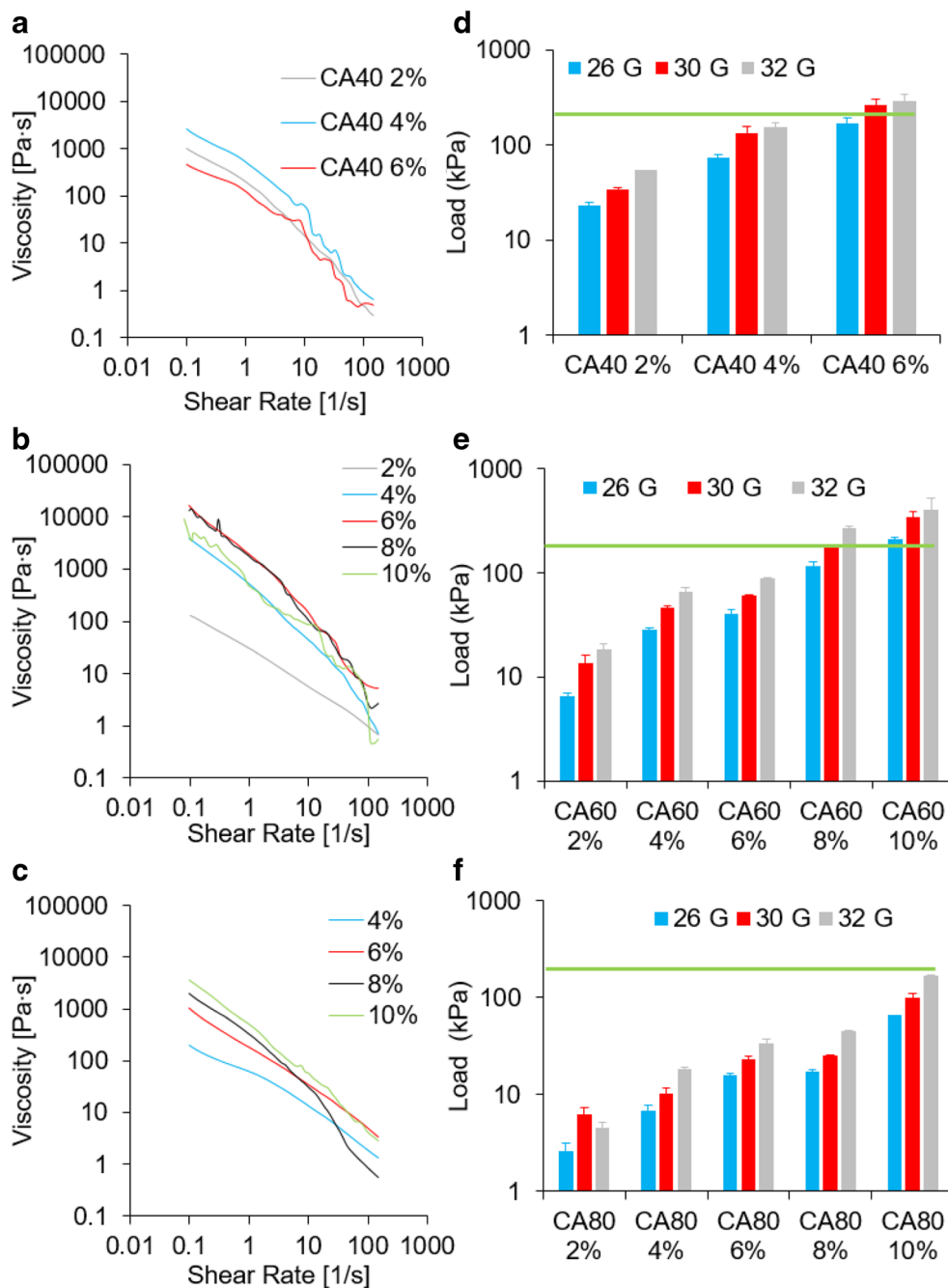
3D bioprinter operating with a maximum pressure of 200 kPa. We measured the load required to extrude a range of CA formulations (SI-Fig. 1D). We then tested several CA formulations, and we identified the highest hydrogel concentration extrudable with all needles within the pressure range of the bioprinter. We found that CA40 could be extruded up to 4% w/v, CA60 up to 6% w/v, and CA80 up to 8% w/v (Fig. 5d–f). These formulations were selected for subsequent testing.

2.6 Extrusion of carboxylated agarose hydrogels at ambient temperature

To obtain precise and consistent bioprinting, the extruded materials need to be of a small but constant diameter. So, the

bioprint quality of hydrogels can be characterized by the extruded material diameter and extrusion consistency. To assess the quality of the previously identify extrudable formulations, we measured the width of the hydrogels extruded with a 32-G needle as a line on a microscope glass slide (Fig. 6a–c). We established that the three formulations gave a similar width between $240 \pm 60 \mu\text{m}$ for the wider CA40 and $140 \pm 25 \mu\text{m}$ for the thinner CA60. However, the standard deviation calculated for ten measurements from three printed lines showed that CA80 was bioprinted with the most reliability at $160 \pm 10 \mu\text{m}$. Having a low width variation during the bioprinting allows us to achieve a precise and reproducible materials deposition, which improves the quality of the bioprinted object.

Fig. 5 Rheological characterization of various concentrations of CA hydrogel showing shear-thinning behavior for **a** CA40, **b** CA60, and **c** CA80. Load required to extrude the CA hydrogels with 26-, 30-, and 32-G needles, showing the maximum hydrogel concentration compatible with conventional 3D bioprinter pressure of 200 kPa (green line) for **d** CA40, **e** CA60, and **f** CA80



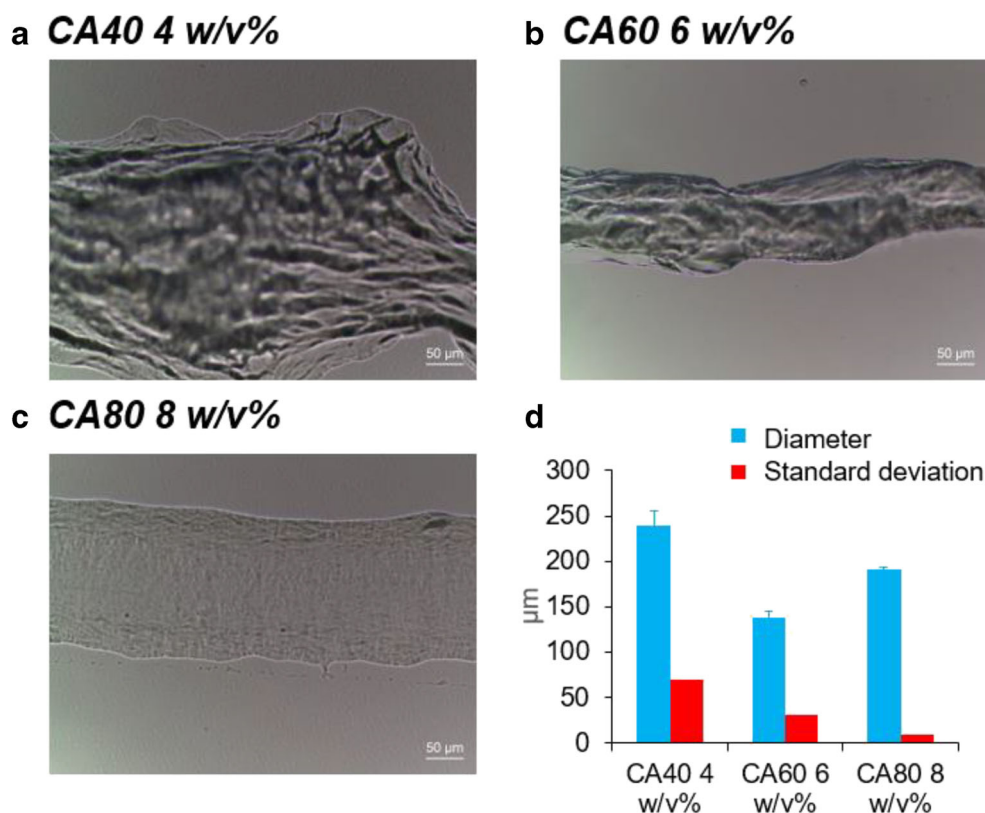
Therefore, 8% CA80 formulation was selected for the subsequent bioprinting.

2.7 Characterization of 3D structures printed at ambient temperature using extrudable carboxylated agarose bioink

Direct conversion of the multimaterial STL file using Slic3r and the slicing method provided by the 3D bioprinter manufacturer did not lead to successful bioprinting as the software cannot reconcile two materials in each layer. Therefore,

particular care had to be taken to avoid collision between the materials during deposition and travel of the printing head. The retraction of the non-printing head had to be adjusted to avoid contact of the non-printing head with the printed object. Also, the travel of each printing head had to be adjusted to correct the non-retraction of the extruder while moving (Fig. 7a). Once the Gcode was modified, the two objects previously designed with a 1-mm and 3-mm vessel diameter were bioprinted with Pluronic F-127 as the fugitive bioink and 8% CA80 as the support bioink for the vessel channel (Fig. 7b, c). For the sake of visualization, the fugitive ink was spiked with

Fig. 6 Microscope pictures of carboxylated agarose (CA) hydrogel formulations extruded on a glass slide with a 32-G needle **a** 4% w/v CA40, **b** 6% w/v CA60, and **c** 8% w/v CA80. **d** Average diameters of a bioprinted line and associated standard deviation for $n = 10$



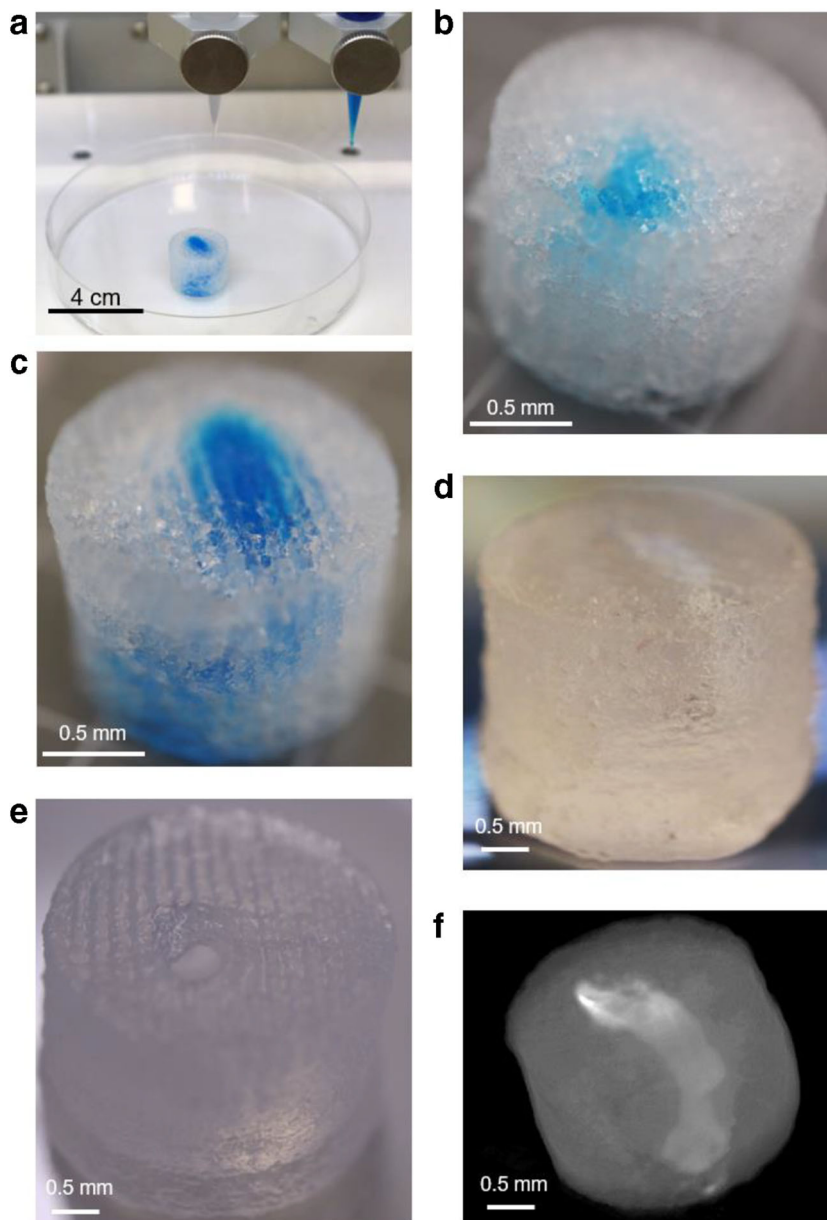
blue-colored food dye. This allowed monitoring any potential contamination and cross deposition of the Pluronic (in blue) in the CA hydrogel during the optimization of the Gcode. Contamination of the CA occurred due to non-retraction of the Pluronic printing head when overlapping the deposited CA. An additional source of contamination was observed when the materials were extruded closely, and the extruded lines were overlapping. Optimization of the Gcode allowed to obtain both hollow channels with 1-mm and 3-mm diameters. The CA extruded at room temperature was clear enough to be able to visualize the colored vessel within the cylinder which was accomplished by using a fugitive phase laden with ink (Fig. 7b, c). After bioprinting, the objects were incubated at 4 °C for 24 h, i.e., below the LCST of Pluronic and lower critical solution temperature (UCST) of CA. This step had a dual purpose of solubilizing the Pluronic while simultaneously consolidating the CA hydrogel phase, thus resulting in a stable cylinder with a hollow vessel. Photomicrographs showing the opening and general direction of the channel is shown in Fig. 7d, e. To ensure entire removal of the Pluronic, the vessel-like structures were rinsed by pipetting cold water in and out of the channel. Although visualizing the entire length and exact path of the hollow channel is challenging due to practical limitations with sectioning large, high aspect ratio hydrated gel structures without causing collapse of the structure; imaging methods such as X-ray computed tomography (μ CT) allow for the 3D reconstruction of biological objects.

This is particularly valuable in characterizing objects created by 3D bioprinting as μ CT offers a non-invasive and non-destructive method to probe the interior, provided that one can establish a contrast between structures of interest. Here, in order to differentiate between the hydrogel and the empty channel, we loaded the channel with a solution of barium sulfate (BaSO_4) which is an approved CT contrast agent for human imaging [29], and thus enabling the direct visualization and confirmation of the hollow channel in 3D space (Fig. 7f).

3 Conclusion

As bioprinting evolves into a reliable processing modality for generating tissue models (organoids) and printed structures containing cells, a new approach for the design of organ models or organ replicates needs to be developed. While copying the architecture of adult organs might provide some information on how a functional organ should be designed, the parametric design offers an approach to liberate us from pre-existing architecture. Using this strategy, we have demonstrated that we can create vessel shapes that resemble natural large vessels found in human anatomy. Therefore, using an algorithm approach for synthetic organ design might allow to improve the function of natural one or creating a design able to counterbalance the limitation of synthetic organs. Finally, we have shown that our design can be bioprinted with

Fig. 7 Printing of 8% w/v 80% carboxylated agarose hydrogel (transparent) at room temperature with Pluronic (blue) as a fugitive ink. **a** Printing of the 1-mm channel and **b** the 3-mm channel and close up photography of the resulting cylinder **c** 1-mm channel printed with the fugitive ink. Photographs of the hollow channel after removal of the fugitive ink **d** 1-mm channel and **e** 3-mm channel. **f** 3-mm hollow channel reconstructed in 3D by μ CT imaging



carboxylated agarose hydrogels at ambient temperature and the dimensional authenticity of the manufactured hollow object can be verified using μ CT. This proposed workflow “from design to validation” represents a new paradigm for realizing complex structures in 3D bioprinting through in silico optimization.

4 Materials and methods

4.1 Parametric design

For the design of the bioprinted objects, Grasshopper plugin was used with Rhinoceros v.5. (Robert McNeel & Associates,

USA). These programs were run on a Dell computer equipped with a Pentium III processor (Intel, USA), 16-GB ram, and internal graphics card. The vessels were created using a generative computer modeling approach. The computational workflow was achieved on Rhinoceros and its visual programming plug-in interface, Grasshopper. The geometric model uses sphere-packing models with minimum-density and maximum-density packing. The algorithm, using an agent-based system behavior, allowed the definition of a desired pore size of the packed internal porous structure. The generation of the vessel and its respective scaffold was computed with a series of custom components written in Python programming language. The results are summarized in (i) scaffolding creation (ii) vessel generation.

4.2 Carboxylated agarose synthesis

One gram of native agarose (NA) type1 (Merck) was transferred into a three-necked round bottom flask, equipped with a mechanical stirrer and pH meter. The reactor was heated to 90 °C to dissolve the agarose and then cooled to 0 °C under mechanically stirring to prevent the solution for gelling. The reactor was then charged with TEMPO (0.160 mmol, 20.6 mg), NaBr (0.9 mmol, 0.1 g), and NaOCl (2.5 mL, 15% vol/vol solution) under vigorous stirring. The pH of the solution was adjusted to pH 10.8 throughout the duration of the reaction, and the degree of carboxylation was controlled by the addition of predetermined volumes of NaOH solution (0.5 M). At the end of the reaction, NaBH₄ (0.1 g) was added, and the solution was acidified to pH 8 and stirred for 1 h. The CA was precipitated by sequential addition of NaCl (0.2 mol, 12 g) and ethanol (500 mL), and the solid was collected by vacuum filtration and extracted using ethanol. Residual ethanol was removed by extensive dialysis against water and the CA was obtained as a white solid upon freeze-drying overnight.

4.3 Rheology

Rheology experiments were performed with a Physica MCR 301 (Anton Paar, Austria) equipped with a Pelletier temperate cell. Samples in deionized water were prepared by heating at 90 °C for 10 min until a clear solution was obtained. The liquid was then poured on to a 6-well plate and allowed to gel at 4 °C for 24 h. A disc of 25 mm was punched out and transferred on the rheometer for analysis. Each curve is a mean of the measurement of three different formulation batches. The test was performed from 0.1 to 150 s⁻¹ and 50 data points per measurement were taken with 6-s interval.

4.4 Mechanical testing

The load required to extrude each carboxylated agarose formulation was measured on a uniaxial mechanical testing machine equipped with a 50 N load cells Instron (USA) and controlled with the BlueHill software (Instron, USA). The printing cartridge equipped with the different printing nozzles (EFD Nordson, Australia) was fixed in alignment with the load cell. The hydrogel was loaded in the cartridge and a wiper piston (EFD Nordson, Australia) was introduced in close contact with the hydrogel. A plunger was 3D printed to be adapted to the load cell and to push the wiper piston. The hydrogel was then extruded at a speed of 30 mm/min and the displacement against load was recorded. The conversion from load to pressure was calculated by measuring the surface area of the wiper piston from the CAD file obtained from the manufacturer.

4.5 3D bioprinting

Bioprinting was conducted on an Inkredible-2 (Cellink, Sweden) 3D printer. The Gcode was created on Slic3r (GNU Affero General Public License) using the parameters provided by the bioprinter manufacturer. The Gcode was then edited on Repetier Host (Hot-World GmbH, Germany).

4.6 Microscopy

Microscopic images of the printed hydrogels were obtained on an optical microscope Axio Scope A1 (Carl Zeiss Microscopy, Germany) and measured with Image J (NIH, USA).

4.7 X-ray tomography

The Pluronic F-127 in the 3D bioprinted objects was removed by incubating the construct at 4 °C for 24 h and followed by flushing the channel 5 times with water. The hollow vessels were coated with a 2% w/v barium sulfate solution and imaged with an X-ray Skyscan μ CT (Bruker, Germany).

4.8 Photography

Pictures of the 3D bioprinted objects were captured on a Canon EOS-M3 camera (Canon, Japan) equipped with a Macro 28-mm objective (Canon, Japan) and were used without further modification.

Acknowledgments The authors wish to thank Florian Miessmer for help with the synthesis of the carboxylated agarose.

Funding information VPS would like to thank the financial support from the Deutscher Akademischer Austauschdienst (DAAD)—German Academic Exchange Service (Grant No. 57319119) and the Excellence Initiative of The German Federal and State Governments (Grant No. EXC 294).

Compliance with ethical standards

Disclaimer The funders had no input in the study and the analysis of the data.

References

1. J.S. Miller, K.R. Stevens, M.T. Yang, B.M. Baker, D.H.T. Nguyen, D.M. Cohen, E. Toro, A.A. Chen, P.A. Galie, X. Yu, R. Chaturvedi, S.N. Bhatia, C.S. Chen, Rapid casting of patterned vascular networks for perfusable engineered three-dimensional tissues. *Nat. Mater.* **11**, 768–774 (2012). <https://doi.org/10.1038/nmat3357>
2. S. Khalil, W. Sun, Bioprinting endothelial cells with alginate for 3D tissue constructs. *J. Biomech. Eng.* **131**, 111002 (2010). <https://doi.org/10.1115/1.3128729>

3. T. Bhattacharjee, S.M. Zehnder, K.G. Rowe, S. Jain, R.M. Nixon, W.G. Sawyer, T.E. Angelini, Supplementary_Writing in the granular gel medium. *Sci. Adv.* **1**, e1500655–e1500655 (2015). <https://doi.org/10.1126/sciadv.1500655>
4. J. Monedero, Parametric design: a review and some experiences. *Autom. Constr.* **9**, 369–377 (2000). [https://doi.org/10.1016/S0926-5805\(99\)00020-5](https://doi.org/10.1016/S0926-5805(99)00020-5)
5. I. Ozbolat, H. Gudapati, A review on design for bioprinting. *Bioprinting* **3**, 1–14 (2016). <https://doi.org/10.1016/j.bprint.2016.11.001>
6. A.A. Zadpoor, Design for additive bio-manufacturing: From patient-specific medical devices to rationally designed meta-biomaterials. *Int. J. Mol. Sci.* **18** (2017). <https://doi.org/10.3390/ijms18081607>
7. K.A. Homan, D.B. Kolesky, M.A. Skylar-Scott, J. Herrmann, H. Obuobi, A. Moisan, J.A. Lewis, Bioprinting of 3D convoluted renal proximal tubules on perfusable chips. *Sci. Rep.* **6**, 34845 (2016). <https://doi.org/10.1038/srep34845>
8. A. Forget, J. Christensen, S. Ludeke, E. Kohler, S. Tobias, M. Matloubi, R. Thomann, V.P. Shastri, S. Lüdeke, E. Kohler, S. Tobias, M. Matloubi, R. Thomann, V.P. Shastri, Polysaccharide hydrogels with tunable stiffness and provasculogenic properties via -helix to -sheet switch in secondary structure. *Proc. Natl. Acad. Sci.* **110**, 12887–12892 (2013). <https://doi.org/10.1073/pnas.1222880110>
9. N. Arya, A. Forget, M. Sarem, V.P. Shastri, RGDSP functionalized carboxylated agarose as extrudable carriers for chondrocyte delivery. *Mater. Sci. Eng. C* **99**, 103–111 (2019). <https://doi.org/10.1016/j.msec.2019.01.080>
10. A. Forget, A. Blaeser, F. Miessmer, M. Köpf, D.F.D. Campos, N.H. Voelcker, A. Blencowe, H. Fischer, V.P. Shastri, Mechanically tunable bioink for 3D bioprinting of human cells. *Adv. Healthc. Mater.* **6**, 1700255–1700262 (2017). <https://doi.org/10.1002/adhm.201700255>
11. A. Sainio, H. Järveläinen, Extracellular matrix macromolecules: potential tools and targets in cancer gene therapy. *Mol. Cell. Ther.* **2**, 14 (2014). <https://doi.org/10.1186/2052-8426-2-14>
12. P. Carmeliet, R.K. Jain, Molecular mechanisms and clinical applications of angiogenesis. *Nature* **473**, 298–307 (2011). <https://doi.org/10.1038/nature10144>
13. A. Neve, F.P. Cantatore, N. Maruotti, A. Corrado, D. Ribatti, Extracellular matrix modulates angiogenesis in physiological and pathological conditions. *Biomed. Res. Int.* **2014**, 1–10 (2014). <https://doi.org/10.1155/2014/756078>
14. J. Li, W. Zhi, T. Xu, F. Shi, K. Duan, J. Wang, Y. Mu, J. Weng, Ectopic osteogenesis and angiogenesis regulated by porous architecture of hydroxyapatite scaffolds with similar interconnecting structure in vivo. *Regen. Biomater.* **3**, 285–297 (2016). <https://doi.org/10.1093/rb/rbw031>
15. H. Mehdizadeh, S. Sumo, E.S. Bayrak, E.M. Brey, A. Cinar, Three-dimensional modeling of angiogenesis in porous biomaterial scaffolds. *Biomaterials* **34**, 2875–2887 (2013). <https://doi.org/10.1016/j.biomaterials.2012.12.047>
16. Q.L. Loh, C. Choong, Three-dimensional scaffolds for tissue engineering applications: role of porosity and pore size. *Tissue Eng. Part B Rev.* **19**, 485–502 (2013). <https://doi.org/10.1089/ten.TEB.2012.0437>
17. P. Lal, W. Sun, Computer modeling approach for microsphere-packed bone scaffold. *CAD Comput. Aided Des.* **36**, 487–497 (2004). [https://doi.org/10.1016/S0010-4485\(03\)00134-9](https://doi.org/10.1016/S0010-4485(03)00134-9)
18. T. Johnson, R. Bahrampourian, A. Patel, K. Mequanint, Fabrication of highly porous tissue-engineering scaffolds using selective spherical porogens. *Biomed. Mater. Eng.* **20**, 107–118 (2010). <https://doi.org/10.3233/BME-2010-0621>
19. Ş. Bora, V. Evren, S. Emek, I. Çakırlar, Agent-based modeling and simulation of blood vessels in the cardiovascular system. *Simulation* **95**, 297–312 (2019). <https://doi.org/10.1177/0037549717712602>
20. J. Jiang, X. Xu, J. Stringer, Support structures for additive manufacturing: a review. *J. Manuf. Mater. Process* **2**, 64 (2018). <https://doi.org/10.3390/jmmp2040064>
21. T.J. Hinton, Q. Jallerat, R.N. Palchesko, J.H. Park, M.S. Grodzicki, H. Shue, M.H. Ramadan, A.R. Hudson, A.W. Feinberg, Three-dimensional printing of complex biological structures by freeform reversible embedding of suspended hydrogels. *Sci. Adv.* **1**, 1–10 (2015). <https://doi.org/10.1126/sciadv.1500758>
22. K. Takagishi, S. Umezu, Development of the improving process for the 3D printed structure. *Sci. Rep.* **7**, 1–10 (2017). <https://doi.org/10.1038/srep39852>
23. L.E. Bertassoni, M. Cecconi, V. Manoharan, M. Nikkha, J. Hjortnaes, A.L. Cristino, G. Barabaschi, D. Demarchi, M.R. Dokmeci, Y. Yang, A. Khademhosseini, Hydrogel bioprinted microchannel networks for vascularization of tissue engineering constructs. *Lab Chip* **14**, 2202–2211 (2014). <https://doi.org/10.1039/c4lc00030g>
24. Amott S, Fulmer A, Scott WE, Dea IC, Moorhouse R, Rees D a (1974) The agarose double helix and its function in agarose gel structure. *J. Mol. Biol.* **90**:269–284
25. A. Forget, R. Gianni-Barrera, A. Uccelli, M. Sarem, E. Kohler, B. Fogli, M.G. Muraro, S. Bichet, K. Aumann, A. Banfi, V.P. Shastri, Mechanically defined microenvironment promotes stabilization of microvasculature, which correlates with the enrichment of a novel Piezo-1⁺ population of circulating CD11b⁺/CD115⁺ monocytes. *Adv. Mater.* **1808050**, 1808050 (2019). <https://doi.org/10.1002/adma.201808050>
26. D.B. Kolesky, R.L. Truby, A.S. Gladman, T.A. Busbee, K.A. Homan, J.A. Lewis, 3D bioprinting of vascularized, heterogeneous cell-laden tissue constructs. *Adv. Mater.* **26**, 3124–3130 (2014). <https://doi.org/10.1002/adma.201305506>
27. A. Rütger, A. Forget, A. Roy, C. Carballo, F. Mießner, R.K. Dukor, L.A. Nafie, C. Johannessen, V.P. Shastri, S. Lüdeke, Unravelling a direct role for polysaccharide β -strands in the higher order structure of physical hydrogels. *Angew Chemie Int. Ed.* **56**, 4603–4607 (2017). <https://doi.org/10.1002/anie.201701019>
28. Naomi Paxton, Willi Smolan, Thomas Böck, Ferry Melchels, Jürgen Groll TJ (2011) Proposal to assess printability of bioinks for extrusion-based bioprinting and evaluation of rheological properties governing bioprintability
29. K.R. Beckett, A.K. Moriarity, J.M. Langer, Safe use of contrast media: what the radiologist needs to know. *RadioGraphics* **35**, 1738–1750 (2015). <https://doi.org/10.1148/rg.2015150033>